Geophysical Journal International

Geophys. J. Int. (2025) **244,** 1–14
Advance Access publication 2025 November 07
Research Paper

https://doi.org/10.1093/gji/ggaf447

A quasi-2-D model of dike propagation with non-equilibrium magma crystallization

Rustam Abdullin [1], Oleg Melnik [2] and Alison Rust[3]

[1] *Department of Theoretical Mechanics, Novosibirsk State University, 2 Pirogova Str, 630090, Novosibirsk, Russia*
[2] *Department of Earth Science, University of Oxford, South Park Road, Oxford, OX1 3AN Oxford, UK. E-mail: oleg.melnik@earth.ox.ac.uk*
[3] *School of Earth Science, University of Bristol, Queen's Road, Bristol, BS8 1RJ Bristol, UK*

Accepted 2025 October 31. Received 2025 October 31; in original form 2025 June 9

SUMMARY

Magma transport in dikes is usually modelled by means of lubrication theory, assuming that magma properties are uniform across the dike. We explore the influence of cross-dike temperature heterogeneity on the dynamics of dike propagation using a quasi-2-D model, derived from a full 2-D model with an assumption of small width to length ratio. The model couples elastic fracture mechanics with multiphase magma flow, solving the governing equations using a hybrid numerical approach that combines the Displacement Discontinuity Method for elasticity with finite volume discretization for fluid flow and heat transfer. The model includes heat exchange with wall rocks, shear heating and latent heat release. It accounts for non-equilibrium magma crystallization, implementing temperature-dependent crystallization kinetics using an Arrhenius formulation for the relaxation timescale. As a case study, we simulate the ascent of a volatile-rich dacite from a source at 30 km depth. The distribution of temperature, crystallinity and, thus, viscosity across the dike leads to a plug-like velocity profile with magma stagnation near the walls, substantially different from the parabolic Poiseuille flow assumed in classical lubrication theory. With temperature-dependent crystallization rate, rapid cooling of magma near the dike walls can generate a glassy chilled margin. The adjacent magma has higher crystallinity due to intermediate cooling rates, while the hotter core remains depleted in crystals throughout dike propagation. The dike propagates further and is thinner than predicted by (1-D) lubrication theory because the low-viscosity core continues to facilitate vertical transport while the wall zones become progressively more viscous due to cooling and crystallization. The latent heat of crystallization can have a substantial impact in slowing down cooling and prolonging propagation. Other important factors include the characteristic crystal growth time, initial magma temperature and water content. Our quasi-2-D approach bridges the gap between oversimplified 1-D models and computationally expensive 3-D simulations, providing a practical framework for investigating magma transport in silicic dikes.

Key words: Lava rheology and morphology; Magma migration and fragmentation; Physics of magma and magma bodies.

1 INTRODUCTION

Dikes are magma-filled fractures that propagate through the lithosphere, playing a critical role in Earth crust formation and magma transport. Thus, predicting dike propagation and emplacement is critical for the understanding of the evolution of magmatic systems and prediction of volcanic eruptions. This study models vertical dike propagation driven by magma buoyancy, although the main findings are also applicable to inclined dikes. We focus on how variations in temperature and crystal content across the dike influence magma propagation and stagnation dynamics. We do not explore the influence of the tectonic settings and topography on dike initiation and magma propagation (Rubin 1995; Gudmundsson 2006; Rivalta *et al.* 2015; Acocella *et al.* 2024; Rivalta & Chamberlain 2025).

All existing 1-D dike models (Lister & Kerr 1991; Roper & Lister 2007; Davis *et al.* 2023) neglect lateral variations in the physical properties of magma, potentially oversimplifying the dynamics of the ascent. Based on the classical analytical Poiseuille solution for the velocity field, these models link analytically the pressure drop along the dike with its thickness, flow rate and viscosity. This assumption is valid for thin dikes where temperature equilibration across the dike happens on timescales that are much shorter, than the timescale of magma propagation or very thick dikes, as the heat loss during their propagation is negligible. Below we show that for a

wide range of parameters, cross-section variations of temperature, crystal content and, thus viscosity have a major control on dike propagation.

The model presented below is based on Abdullin *et al.* (2024) that incorporated volatile exsolution, equilibrium crystallization and heat exchange with wall rocks. They found that due to degassing-induced crystallization governed by the liquidus temperature increase as a consequence of water exsolution, the dike propagation slows down, magma progressively cools and crystallize and, finally, becomes arrested. For a given magma composition and a source depth, the ascent rate and arrest depth depend on, among other factors, the amount of magma injected into the dike at depth, and its initial volatile content and temperature.

In this study, we extend the model of Abdullin *et al.* (2024) to a 2-D framework to account for variations in physical parameters across the width of the dike to investigate the impact of crystallization kinetics, latent heat and melt viscosity variations on dike propagation dynamics.

We develop and validate an efficient numerical algorithm based on the Displacement Discontinuity Method (DDM) and a finite volume scheme to enhance our understanding of magma transport in silicic systems that, for example lead to formation of as porphyry-type ore deposits (Carter *et al.* 2021). To facilitate comparison with results of Abdullin *et al.* (2024), we use the same volatile-saturated dacitic magma composition and the same reference values of model parameters. This includes a very deep source depth of 30 km, originally motivated by geochemical evidence for deep, wet sources for hypabyssal intrusions associated with economic porphyry ore deposits.

This paper is organized as follows. Section 2 formulates the governing equations based on elastic response of surrounding rock. Magma flow is described by Navier–Stokes equations. We subsequently provide a simplified version of these equations. Section 2.4 presents the balance equations for the different phases in magma and details the magma rheology. Section 3 describes the numerical implementation of the model. Section 4 provides results of a quasi-2-D simulations and compares with the 1-D case. Finally, Appendix A provides details on the simplification of the Navier–Stokes equations used in the model.

2 MATHEMATICAL MODEL FOR A MAGMA ASCENT

This section presents the governing equations for magma transport through a vertical dike, modelled as a planar fracture that propagates upward due to buoyancy. The magma is treated as a multiphase medium, incorporating volatile species (H_2O and CO_2) and crystals growing due to decompression and cooling of the magma. We allow physical parameters such as viscosity and temperature to vary both vertically along the dike and horizontally across its width. We also assume that the width of the dike is much smaller than its length.

2.1 Dike propagation equations

The dike propagates in the vertical direction x into an elastic medium (see Fig. 1). Let w denote the fracture width and p the magma pressure. Assuming symmetry with respect to the vertical x-axis, we restrict our analysis to the left half-plane. The dike domain is bounded by $y = 0$ and $y = h(x, t)$, where $h = w/2$ is the fracture half-width.

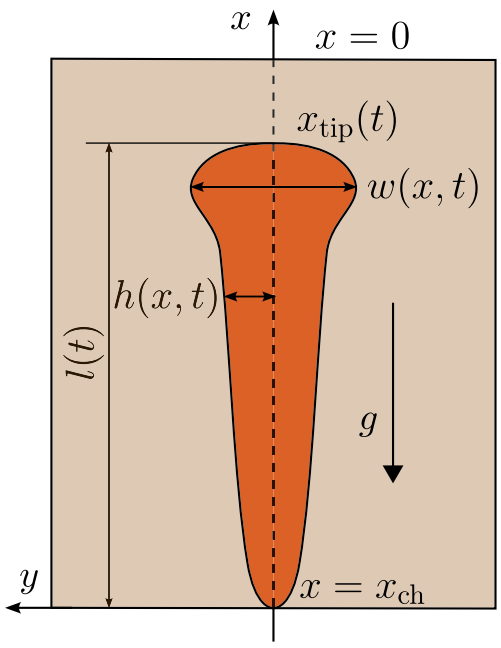

Figure 1. Schematic illustration of dike (darker colour) propagating vertically along the x-axis. The fracture extends from the inlet at $x = x_{ch}$ to the current tip position at $x = x_{tip}(t)$, with total length $l(t)$. The fracture width is denoted by $w(x, t)$, and the half-width by $h(x, t) = w(x, t)/2$. Note that the lateral extent of the host rock is greater than shown, so that boundary effects do not influence the dike.

To simplify the mathematical formulation, we define separate coordinate systems for the magma and the surrounding host rock. The vertical x-axis is shared by both systems, while the y-axis origin differs:

(i) For the magma inside the dike: the origin is at the centreline of the dike (the symmetry axis).
(ii) For the host rock: the origin is located at the dike wall $y = h(x, t)$.

The integral equation of linear elasticity relates the fracture opening w to the normal stress change along the dike—from its ambient value σ_0 to the current value governed by the magma pressure p and the cohesive stress σ_{coh}:

$$p(x, t) = \sigma_0(x) + \sigma_{coh}(w(x, t)) - \frac{E'}{4\pi} \int_{x_{ch}}^{x_{tip}(t)} \frac{\partial w(s, t)}{\partial s} \frac{\mathrm{d}s}{s - x}, \qquad (1)$$

where $E' = E/(1 - \nu^2)$ is the plane strain modulus, x_{ch} is the depth of the magma chamber (source) and $x_{tip}(t)$ is the position of the dike tip. A cohesive zone model is employed for the propagation condition. The cohesive stress weakens as the fracture opening increases, decreasing linearly from its peak value σ_c at $w = 0$ to zero at or above the critical cohesive fracture opening $w \geq w_c$ (Golovin & Baykin 2018; Garagash 2019). The following linear law for the cohesive stress is used

$$\sigma_{coh}(w) = \begin{cases} \sigma_c \left(1 - \dfrac{w}{w_c}\right), & 0 \leqslant w \leqslant w_c, \\ 0, & w > w_c. \end{cases} \qquad (2)$$

Equating the work of the cohesive stress to Griffith's fracture energy $G_c = \int_0^\infty \sigma_{coh}(w)\,\mathrm{d}w$ (Griffith 1921) gives $w_c = 2G_c/\sigma_c$. For sufficiently long fractures, the fracture energy is related to the fracture

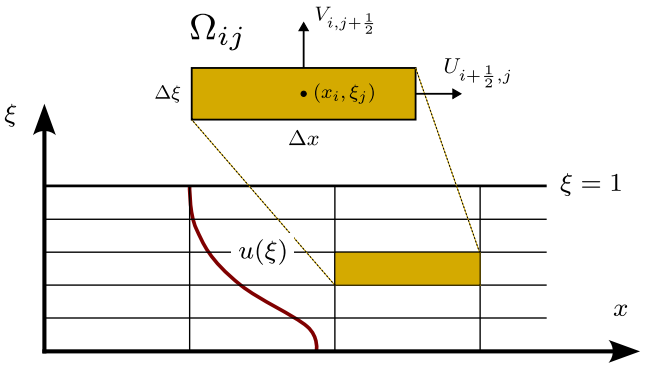

Figure 2. Structured rectangular mesh used to discretize the magma domain.

toughness K_{Ic} via Irwin's formula (Irwin 1957): $K_{Ic} = \sqrt{\frac{EG_c}{1-\nu^2}}$. The cohesive strength σ_c can be adjusted to control the cohesive zone length in the numerical simulations (Baykin *et al.* 2023).

We note that eq. (1) does not strictly satisfy the traction-free boundary condition at $x = 0$ (Roper & Lister 2005). However, for sufficiently long dikes originating from deep magma sources, the influence of the free surface is negligible (Dontsov 2016). In this work, we neglect tectonic contributions to the ambient stress (Rubin 1995) and assume it to be purely lithostatic: $\sigma_0 = p_{\text{lith}}(x)$, where the lithostatic pressure is given by $p_{\text{lith}}(x) = \int_x^0 \rho_r(s) g \, \mathrm{d}s$.

2.2 Magma flow equations

We define the phase volume fractions as follows: α_g and α_d represent the volume fractions of exsolved and dissolved gas, respectively; α_m corresponds to the liquid melt fraction; and α_c denotes the fraction of solid crystals. In this study, following arguments in Abdullin *et al.* (2024) we assume that the relative velocity between gas bubbles and melt is negligible, enabling us to treat the entire multiphase magma as sharing a single velocity field. Under this assumption, the mass conservation law for each phase takes the form:

$$\frac{\partial \alpha_N \rho_N}{\partial t} + \nabla \cdot (\alpha_N \rho_N \boldsymbol{u}) = \mathcal{I}_N, \tag{3}$$

where $\boldsymbol{u} = (u, v)$ is the magma flow velocity field, with u and v representing the velocities in the vertical (x) and transversal (y) directions respectively, and ρ_N is the density of phase N for $N = g, d, m, c$. $\mathcal{I}_N$ is the rate of mass transfer to the phase N from the other phases per unit total volume.

With the assumption of identical velocities across all phases, the conservation laws can be expressed in terms of the bulk magma density $\rho = \sum_N \alpha_N \rho_N$

$$\frac{\partial \rho}{\partial t} + \nabla \cdot (\rho \boldsymbol{u}) = 0, \tag{4}$$

$$\frac{\partial \rho \boldsymbol{u}}{\partial t} + \nabla \cdot (\rho \boldsymbol{u}\boldsymbol{u}) = -\nabla p + \rho \boldsymbol{g} + \nabla \cdot \boldsymbol{\tau}, \tag{5}$$

$$\frac{\partial (\rho C T)}{\partial t} + \nabla \cdot (\rho C T \boldsymbol{u}) = \nabla \cdot (k \nabla T) + \boldsymbol{\tau} : \nabla \boldsymbol{u} + \Phi_c. \tag{6}$$

In these equations, $\boldsymbol{u}\boldsymbol{u}$ denotes the outer product of the velocity vector, $\boldsymbol{g} = (-g, 0)$ is the gravitational acceleration, C is the specific heat capacity, T is temperature and k is the thermal conductivity of the magma. Here, $\nabla\cdot$ and ∇ denote the divergence and gradient operators, respectively.

To describe the viscous response of the magma, we assume a Newtonian rheology where the shear stress tensor $\boldsymbol{\tau}$ is related to the strain rate as:

$$\boldsymbol{\tau} = \mu \left[\nabla \boldsymbol{u} + (\nabla \boldsymbol{u})^T \right], \tag{7}$$

where μ is the magma viscosity, which depends on temperature, dissolved volatile content and crystallinity. The functional form of μ is detailed in Section 2.4. The term $\boldsymbol{\tau} : \nabla \boldsymbol{u}$ in eq. (6) accounts for viscous dissipation (shear heating) during magma flow (Rubin 1995). The final term, Φ_c, represents the latent heat released during crystallization:

$$\Phi_c = L^* \left[\frac{\partial (\alpha_c \rho_c)}{\partial t} + \nabla \cdot (\alpha_c \rho_c \boldsymbol{u}) \right] = L^* \mathcal{I}_c. \tag{8}$$

Boundary conditions are imposed to reflect symmetry at the dike centreline $y = 0$ and no-slip behaviour at the fracture wall $y = h(x, t)$:

$$\begin{aligned} rlly = 0: \quad & \frac{\partial u}{\partial y} = 0, \, v = 0, \\ y = h(x,t): \quad & u = 0, \, v = \frac{\partial h}{\partial t}. \end{aligned} \tag{9}$$

The inflow of magma from the chamber is characterized by the source mass flux Q_m at $x = x_{\text{ch}}$:

$$Q_m = 2 \int_0^{h(x_{\text{ch}},\, t)} \rho u \, \mathrm{d}y. \tag{10}$$

To determine the temperature field T_r in the surrounding host rock, we consider the heat conduction equation:

$$\frac{\partial (\rho_r C_r T_r)}{\partial t} = \nabla \cdot (k_r \nabla T_r), \tag{11}$$

where C_r and k_r denote the specific heat capacity and the thermal conductivity of the host rock, respectively. The initial thermal state of the host rock is prescribed by the geothermal gradient, assumed as a linear function of depth:

$$T_r^0(x) = T_0 + Gx, \tag{12}$$

where T_0 is the reference surface temperature and G is the constant geothermal gradient. At the outer boundary $y = L_r$, a Dirichlet condition is imposed:

$$T_r(x,t)|_{y=L_r} = T_r^0(x). \tag{13}$$

The domain size L_r is selected large enough to prevent boundary effects from influencing the solution near the dike.

At the dike wall $y = h(x, t)$, thermal continuity conditions are enforced for both temperature and heat flux:

$$\begin{aligned} T\big|_{y=h(x,t)} &= T_r\big|_{y_r=0}, \\ k \frac{\partial T}{\partial y}\bigg|_{y=h(x,t)} &= k_r \frac{\partial T_r}{\partial y_r}\bigg|_{y_r=0}. \end{aligned} \tag{14}$$

At the symmetry axis $y = 0$, a zero heat flux (Neumann) condition is imposed:

$$\frac{\partial T}{\partial y}\bigg|_{y=0} = 0. \tag{15}$$

2.3 Simplified governing equations

To reduce the system, we assume a low Reynolds number regime ($Re = \rho u w / \mu$), appropriate for highly viscous, silica-rich magmas. Under this assumption, inertial effects are negligible. The full

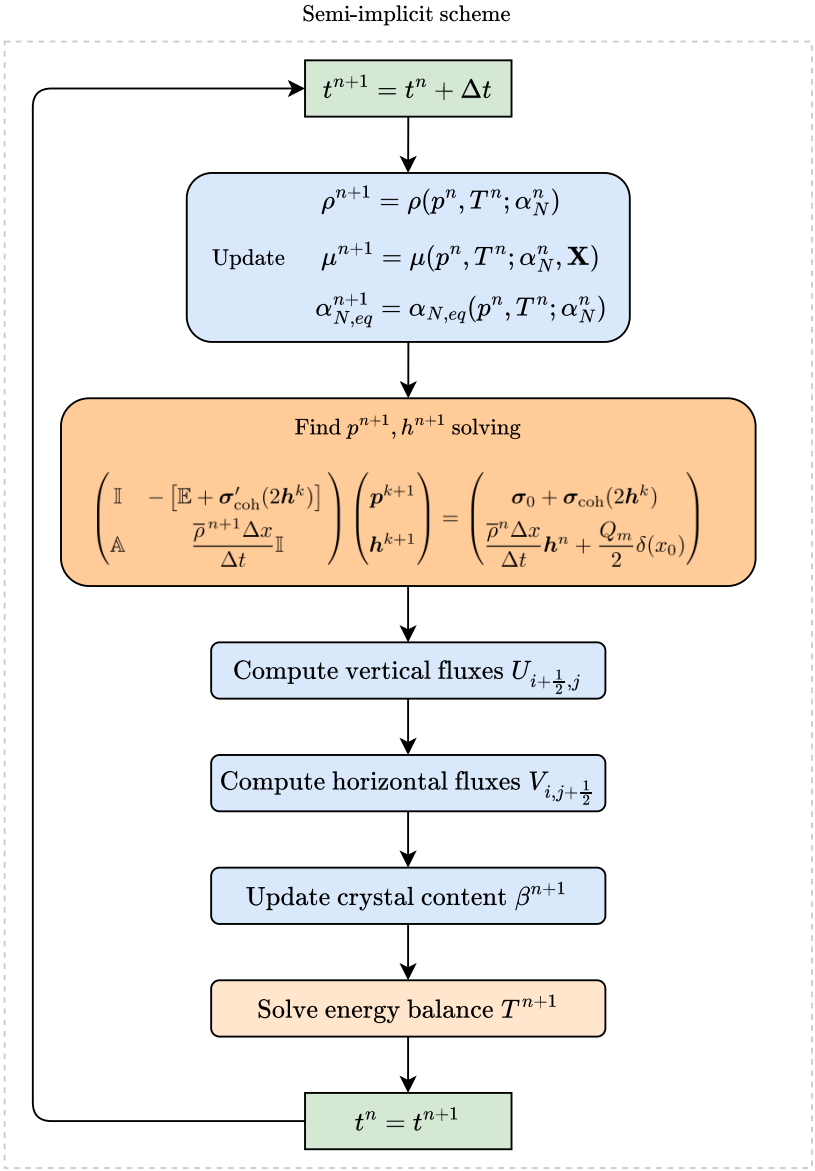

Figure 3. Computational algorithm for the coupled magma propagation model used in this study.

derivation is provided in Appendix A, and the resulting simplified eqs (4)–(6) are:

$$\frac{\partial \rho}{\partial t} + \frac{\partial (\rho u)}{\partial x} + \frac{\partial (\rho v)}{\partial y} = 0, \tag{16}$$

$$-\frac{\partial p}{\partial x} - \rho g + \frac{\partial}{\partial y}\left(\mu \frac{\partial u}{\partial y}\right) = 0, \tag{17}$$

$$\frac{\partial (\rho C T)}{\partial t} + \frac{\partial (\rho C T u)}{\partial x} + \frac{\partial (\rho C T v)}{\partial y} = \frac{\partial}{\partial y}\left(k \frac{\partial T}{\partial y}\right) + \mu \left(\frac{\partial u}{\partial y}\right)^2 + \Phi_c. \tag{18}$$

Note that the momentum balance for the transverse velocity component v reduces to $\frac{\partial p}{\partial y} = 0$, implying that the pressure depends only on the vertical coordinate: $p = p(x, t)$.

In eq. (18), the conductive term $k\nabla T$ is approximated by $k\frac{\partial T}{\partial y}$, justified by the high aspect ratio (length $\gg$ width) of the dike. Similarly, the host rock conduction eq. (11) simplifies to:

$$\frac{\partial (\rho_r C_r T_r)}{\partial t} = \frac{\partial}{\partial y}\left(k_r \frac{\partial T_r}{\partial y}\right). \tag{19}$$

2.4 Magma properties

This subsection introduces the equations that govern phase transitions within magma and describes how magma viscosity is modelled. Because dissolved volatile concentrations are typically expressed in mass fractions, we adopt a notation consistent with previous studies (Melnik & Sparks 1999, 2002; Abdullin *et al.* 2024).

We define α as the volume fraction of exsolved gas (bubbles), and β as the volume fraction of crystals in the bubble-free melt. The variables $c_{\mathrm{H_2O}}$ and $c_{\mathrm{CO_2}}$ denote the mass fractions of dissolved water and carbon dioxide in the melt, respectively. The phase volume and mass fractions satisfy the following relations:

Table 1. Model parameters and their reference values

Parameter	Description	Reference value	Units
C	Specific heat capacity of magma	1200	J (kg · K)$^{-1}$
C_r	Specific heat capacity of host rock	1200	J (kg· K)$^{-1}$
$c_{\mathrm{H_2O,ch}}$	Initial dissolved water content	6.18	wt per cent
E	Young's modulus of host rock	20	GPa
E_a	Activation energy for relaxation time	210	kJ mol^{-1}
G	Geothermal gradient	30	°C km^{-1}
g	Acceleration due to gravity	9.81	m s^{-2}
K_{Ic}	Fracture toughness	1	MPa· m$^{1/2}$
k	Thermal conductivity of magma	2	W (m· K)$^{-1}$
k_r	Thermal conductivity of host rock	2	W (m· K)$^{-1}$
L^*	Latent heat of crystallization	350	kJ kg^{-1}
N_y	Number of cells in transverse direction	30	–
Q_m	Source magma mass flux per unit breadth	2000	kg (m· s)$^{-1}$
T_0	Reference surface temperature	0	°C
T_{ch}	Initial magma temperature	900	°C
τ_0	Pre-exponential factor for crystal relaxation	1×10^{-6}	s
t_{ch}	Injection duration (non-zero Q_m)	15000	s
Δx	Cell size in vertical direction	100	m
x_{ch}	Depth of magma chamber	30	km
ν	Poisson's ratio of rock	0.25	–
ρ_c	Density of crystalline phase	2700	kg m^{-3}
$\rho_{d,\mathrm{CO_2}}$	Density of dissolved carbon dioxide	1400	kg m^{-3}
$\rho_{d,\mathrm{H_2O}}$	Density of dissolved water	900	kg m^{-3}
$\rho_{m,\mathrm{liq}}$	Density of liquid melt phase	2360	kg m^{-3}
ρ_r	Host rock density	2700	kg m^{-3}

$$\alpha_g = \alpha, \tag{20}$$

$$\alpha_c = (1-\alpha)\beta, \tag{21}$$

$$\alpha_d \rho_d = (1-\alpha)(1-\beta)(c_{\mathrm{H_2O}} + c_{\mathrm{CO_2}})\rho_m, \tag{22}$$

$$\alpha_l \rho_l = (1-\alpha)(1-\beta)(1 - c_{\mathrm{H_2O}} - c_{\mathrm{CO_2}})\rho_m. \tag{23}$$

The density of the liquid melt ρ_m is computed from the partial contributions of its dissolved constituents:

$$\rho_m = 1 \Big/ \left(\frac{c_{\mathrm{H_2O}}}{\rho_{d,\,\mathrm{H_2O}}} + \frac{c_{\mathrm{CO_2}}}{\rho_{d,\,\mathrm{CO_2}}} + \frac{1 - c_{\mathrm{H_2O}} - c_{\mathrm{CO_2}}}{\rho_{m,\,\mathrm{liq}}} \right) \tag{24}$$

In this expression, $\rho_{d,\,\mathrm{H_2O}}$ and $\rho_{d,\,\mathrm{CO_2}}$ denote the densities of water and carbon dioxide dissolved in the melt, while $\rho_{m,\,\mathrm{liq}}$ is the density of the volatile-free melt. To determine fluid saturation conditions in the H_2O–CO_2 system, we use the MagmaSat model of Ghiorso & Gualda (2015), implemented within the VESIcal software package (Iacovino *et al.* 2021).

The evolution of the crystal content is governed by the mass balance eq. (3). Degassing-induced crystallization is modelled using as a simplified first-order kinetic law (La Spina *et al.* 2015; Tsepelev *et al.* 2020):

$$\mathcal{I}_c = -\mathcal{I}_l = -(1-\alpha)\rho_c \frac{\beta - \beta_{\mathrm{eq}}}{\tau_c}, \tag{25}$$

where β_{eq} is the equilibrium crystal volume fraction, and τ_c is the characteristic time required for the crystal content to approach equilibrium. While previous studies (La Spina *et al.* 2015; Tsepelev *et al.* 2020) used a constant value for τ_c, we adopt a temperature-dependent Arrhenius formulation:

$$\tau_c = \tau_0 \exp\left(\frac{E_a}{RT}\right), \tag{26}$$

where τ_0 is a reference timescale, E_a is the activation energy, T is the magma temperature (in K) and $R = 8.314\,\mathrm{J\,(mol \cdot K)^{-1}}$ is the universal gas constant. The value of the activation energy E_a depends on the magma composition and minerals that are growing. As crystallization involves diffusion of major elements towards and away from crystal-melt interfaces, the value of E_a should be the same order as activation energies of network-forming cations (Si, Al) and network-modifiers (Na, K, Ca, Mg, Fe). Typical ranges of E_a are of the order of 100–250 kJ mol^{-1} (Zhang *et al.* 2010). In this paper, we chose a representative value of 200 kJ mol^{-1}.

This formulation accounts for the enhanced crystallization rate at higher temperatures. See Fig. S2 of the Supplementary Materials for a plot of the temperature dependence of τ_c for $\tau_0 = 10^{-6}$ s. This value gives characteristic equilibration times of ∼ 15 min at 950 °C to 7 hr at 780 °C (the value of the storage temperature of Pinatubo magma; Hammer & Rutherford 2002). Total crystallization time will be longer as the growth rate decreases at low degrees of magma supersaturation.

Following Abdullin *et al.* (2024), the equilibrium crystallinity, liquidus and solidus are based on fits to data from laboratory experiments. The equilibrium crystallinity, β_{eq} is expressed as a function of the reduced temperature $T' = (T - T_S)/(T_L - T_S)$:

$$\beta_{\mathrm{eq}} = \left[1 + \exp\left(a_F + b_F T' + c_F T'^2 + d_F T'^3\right)\right]^{-1}, \tag{27}$$

with fitted coefficients $a_F = -4.974$, $b_F = 28.623$, $c_F = -52.708$ and $d_F = 34.816$.

The liquidus (T_L) and solidus (T_S) temperatures are modelled as functions of pressure p (in kbar) and water molar fraction $X_{\mathrm{H_2O}}$:

$$T_L = a_L + b_L p - X_{\mathrm{H_2O}}\left(c_L + f_L p - \frac{d_L}{p + e_L}\right) + \Delta T_L, \tag{28}$$

$$T_S = a_S + b_S p - X_{\mathrm{H_2O}}\left(c_S + f_S p - \frac{d_S}{p + e_S}\right), \tag{29}$$

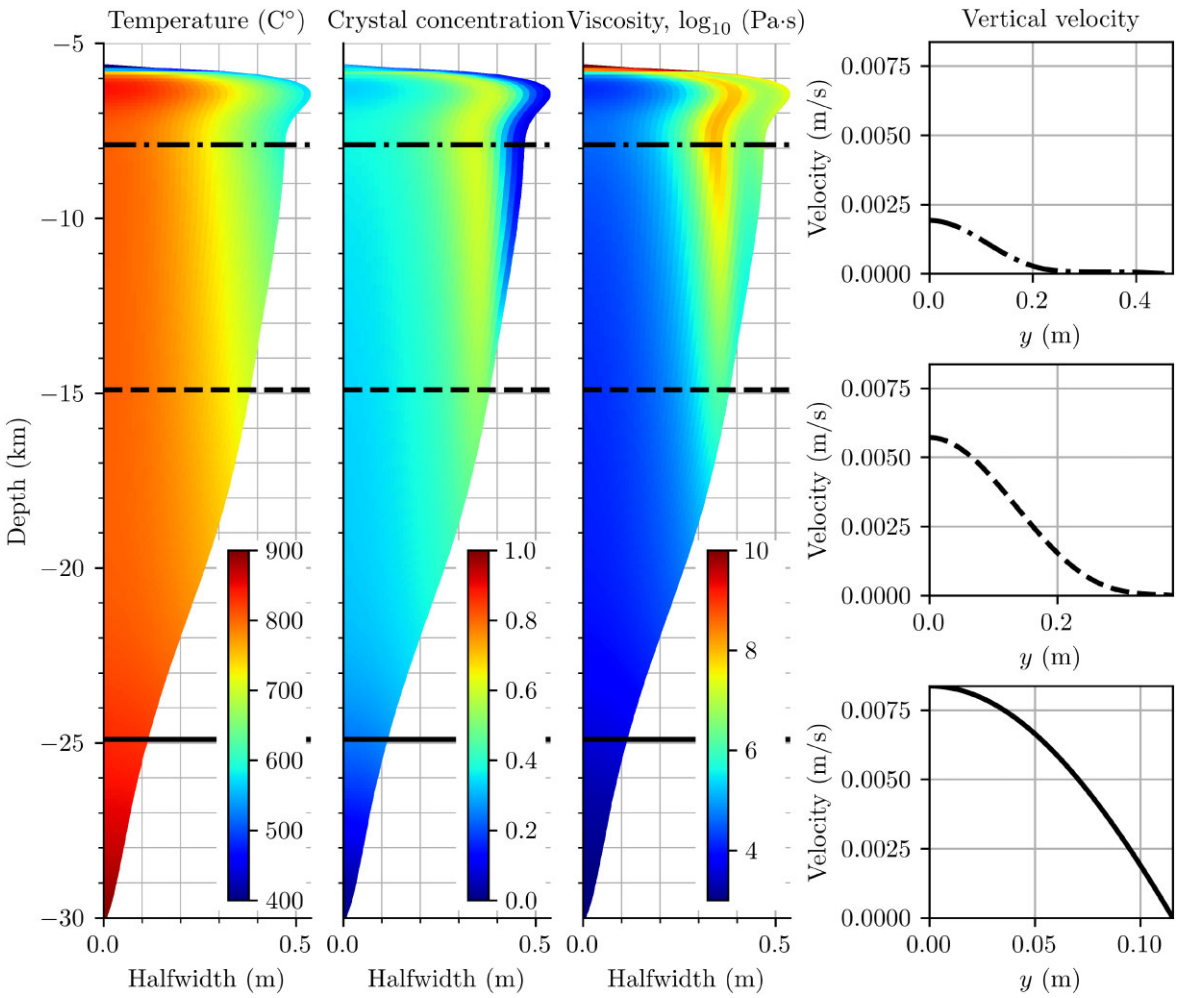

Figure 4. The propagation of a dike based on the implemented algorithm at approximately 44.4 hr after injection initiation. Panels from left to right show temperature distribution, crystal concentration, viscosity and vertical velocity profiles at selected depths indicated by horizontal lines: solid (25 km), dashed (15 km) and dash-dotted (8 km). The simulation employs the kinetic law (26) with $\tau_0 = 10^{-6}$ s (Fig. S2, Supplementary Materials) and the parameters from Table 1.

where $X_{H_2O} = C_{H_2O}/(C_{H_2O} + C_{CO_2})$. The empirical coefficients in eqs (28)–(29) are:

(i) Liquidus: $a_L = 1205.7$, $b_L = 6.0$, $c_L = 285.7$, $d_L = 200.0$, $e_L = 0.7$, $f_L = 11.0$,
(ii) Solidus: $a_S = 854.1$, $b_S = 6.0$, $c_S = 224.1$, $d_S = 80.0$, $e_S = 0.36$, $f_S = 6.0$.

The term $\Delta T_L = 1287.6 - 20.15 \cdot SiO_2$ accounts for compositional correction based on silica content (in wt. per cent).

Magma viscosity μ depends on temperature T and melt composition $\boldsymbol{X}$, with a strong sensitivity to dissolved water content c_{H_2O} (Abdullin *et al.* 2024). It is modelled as:

$$\mu = \mu_m(T, \boldsymbol{X}) \cdot \theta(\beta), \tag{30}$$

where $\mu_m(T, \boldsymbol{X})$, evaluated using the model of Giordano *et al.* (2008). The effect of crystals on the bulk magma viscosity is captured by the function $\theta(\beta)$, defined as (Costa *et al.* 2009):

$$\theta(\beta) = \phi(\beta) \cdot \frac{1 + \left(\frac{\beta}{\beta_*}\right)^{\delta}}{\left(1 - \varepsilon \operatorname{erf}\left\{\frac{\sqrt{\pi}\beta}{2\varepsilon\beta_*}\left[1 + \frac{\beta}{\beta_*}\right]^{\gamma}\right\}\right)^{2.5\beta_*}}. \tag{31}$$

The function $\phi(\beta)$ accounts for compositional changes associated with crystal growth (Dirksen *et al.* 2006):

$$\phi(\beta) = \exp\left[a_1(\beta - \beta_{ch}) + a_2(\beta - \beta_{ch})^2\right]. \tag{32}$$

In this study following Dirksen *et al.* (2006), we use the following parameters: $\beta^* = 0.67$, $\gamma = 3.99$, $\delta = 16.94$, $\varepsilon = 0.999916$, $a_1 = 4.33$ and $a_2 = 10.48$. A more accurate calibration for particular magma composition can be achieved by linking the code with thermodynamic software, for example, rhyolite Melts (Ghiorso & Gualda 2015).

3 NUMERICAL METHOD

This section outlines the numerical implementation of the governing equations for magma flow and fracture propagation, as introduced in the previous section. Due to the time-dependent variation in dike half-width, we introduce a moving coordinate system:

$$\begin{cases} \tilde{t} = t, \\ \tilde{x} = x, \\ \xi = \dfrac{y}{h(x,t)}. \end{cases} \tag{33}$$

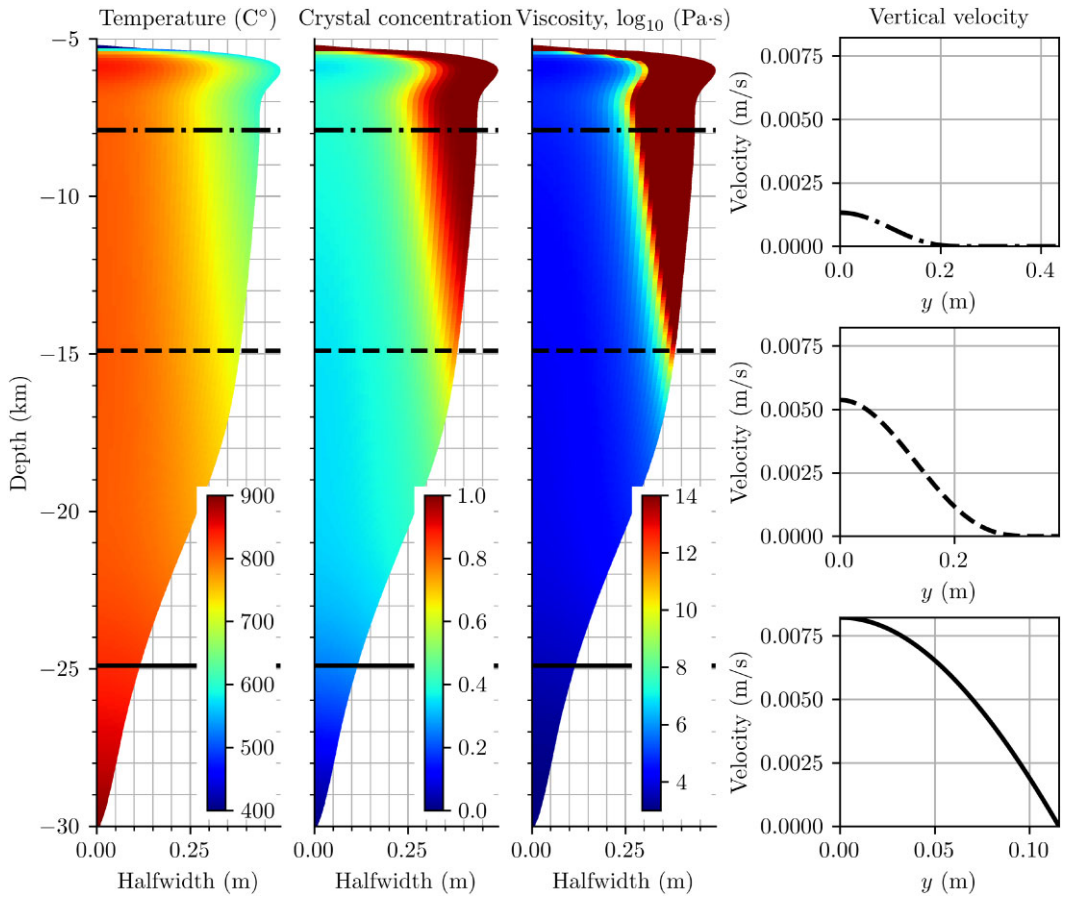

Figure 5. Dike propagation at approximately 44.4 hr after injection initiation, using constant relaxation crystallization model with $\tau_c = 20$ s. This short timescale means the crystalinities are approximately equilibrium values. Panels from left to right show temperature distribution, crystal concentration, viscosity and vertical velocity profiles at selected depths indicated by horizontal lines: solid (25 km), dashed (15 km) and dash-dotted (8 km).

In these new coordinates, the magma domain is confined within the interval $\xi \in [0, 1]$. Applying the chain rule for partial differentiation, we obtain the following transformation relations:

$$\begin{cases} \dfrac{\partial}{\partial t} = \dfrac{\partial}{\partial \tilde{t}} - \dfrac{\xi h_t}{h}\dfrac{\partial}{\partial \xi}, \\ \dfrac{\partial}{\partial x} = \dfrac{\partial}{\partial \tilde{x}} - \dfrac{\xi h_x}{h}\dfrac{\partial}{\partial \xi}, \\ \dfrac{\partial}{\partial y} = \dfrac{1}{h}\dfrac{\partial}{\partial \xi}. \end{cases} \tag{34}$$

This transformation maps the physical domain onto a fixed computational domain, such that the dike wall remains at $\xi = 1$. This simplifies the enforcement of boundary conditions and the numerical discretization procedure.

Applying this coordinate transformation to eqs (16)–(18) yields the following transformed system:

$$\frac{\partial(\rho h)}{\partial \tilde{t}} + \frac{\partial(\rho h u)}{\partial \tilde{x}} + \frac{\partial(\rho \widehat{v})}{\partial \xi} = 0, \tag{35}$$

$$-\frac{\partial p}{\partial \tilde{x}} - \rho g + \frac{1}{h^2}\frac{\partial}{\partial \xi}\left(\mu \frac{\partial u}{\partial \xi}\right) = 0, \tag{36}$$

$$\frac{\partial(\rho C T h)}{\partial \tilde{t}} + \frac{\partial(\rho C T h u)}{\partial \tilde{x}} + \frac{\partial(\rho C T \widehat{v})}{\partial \xi} = \frac{1}{h}\frac{\partial}{\partial \xi}\left(k\frac{\partial T}{\partial \xi}\right) + \frac{\mu}{h}\left(\frac{\partial u}{\partial \xi}\right)^2 + h\Phi_c, \tag{37}$$

where $\widehat{v} = v - \xi h_t - \xi h_x u$. Eqs (16) and (18) are multiplied by h to avoid division by zero and to simplify the transformed expressions. For notational clarity, we omit tildes on $\tilde{t}$ and $\tilde{x}$ in what follows.

The symmetry condition at $\xi = 0$ and the no-slip boundary at the dike wall ($\xi = 1$) translate into the following conditions:

$$\begin{aligned} &\xi = 0 : \frac{\partial u}{\partial \xi} = 0, \ \widehat{v} = 0, \\ &\xi = 1 : u = 0, \quad \widehat{v} = 0. \end{aligned} \tag{38}$$

Integrating the mass conservation eq. (35) over the transverse coordinate $\xi \in [0, 1]$, we obtain:

$$\frac{\partial \overline{\rho} h}{\partial t} + \frac{\partial \overline{q} h}{\partial x} = 0, \tag{39}$$

where $\overline{\rho} = \int_0^1 \rho \, \mathrm{d}\xi$ and $\overline{q} = \int_0^1 \rho u \, \mathrm{d}\xi$ are the mean density and vertical mass rate, respectively.

The numerical method employed combines the Displacement Discontinuity Method (Crouch *et al.* 1983) for solving the elasticity eq. (1) with a modified finite volume method for magma flow (eqs 35–37). The domain is discretized using a structured rectangular mesh in both the vertical (x) and transverse (ξ) directions, as illustrated in Fig.2 The x-axis is divided into N_x segments of length Δx with centres at x_i, and the interval [0,1] in the ξ-direction is partitioned into N_y segments of length $\Delta\xi$ with centres at ξ_j. Each control volume Ω_{ij} is centred at (x_i, ξ_j), and cell-averaged values

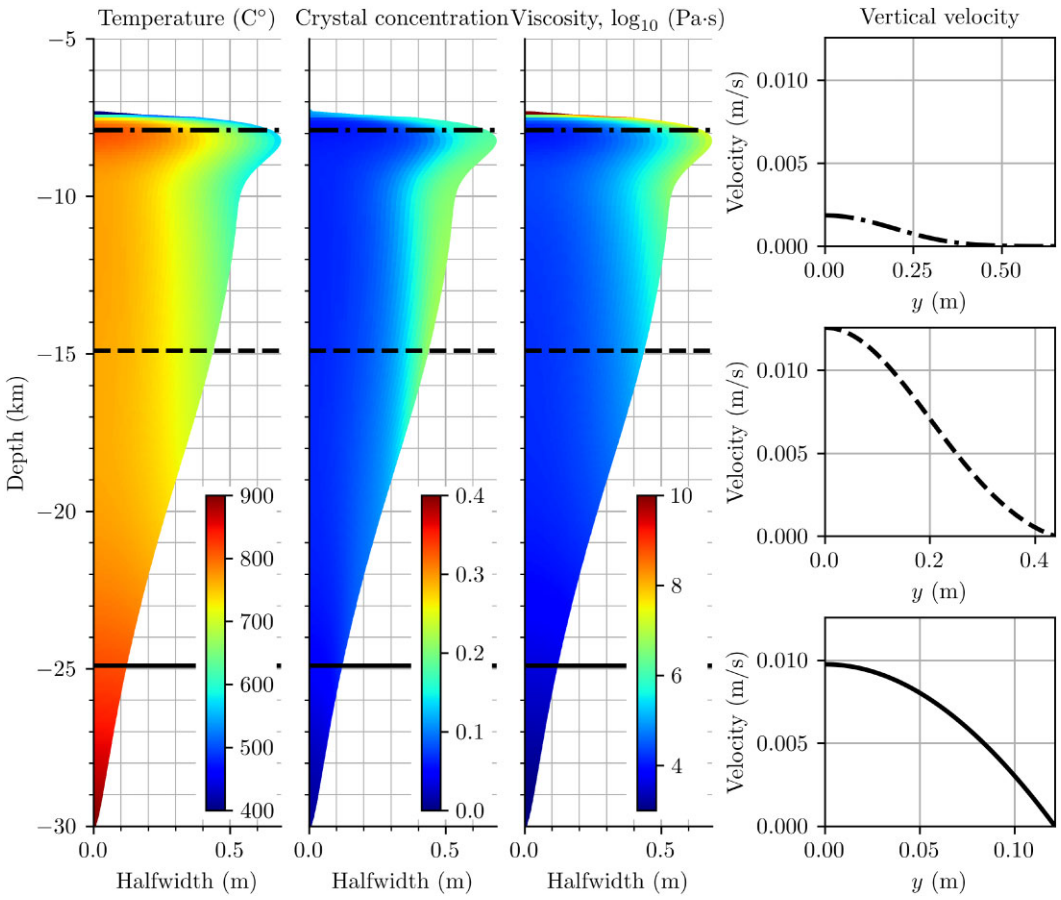

Figure 6. Dike propagation at approximately 44.4 hr after injection initiation, using constant relaxation crystallization model with $\tau_c = 1$ week. Panels from left to right show temperature distribution, crystal concentration, viscosity and vertical velocity profiles at selected depths indicated by horizontal lines: solid (25 km), dashed (15 km) and dash-dotted (8 km).

of magma properties—such as pressure, temperature, density and viscosity—are stored at these locations.

Integrating the mass conservation eq. (35) over the control volume Ω_{ij} gives:

$$\begin{aligned}&\frac{(\rho_{ij}h_i)^{n+1}-(\rho_{ij}h_i)^n}{\Delta t}\Delta x\,\Delta\xi+(\rho U)^{n+1}_{i+\frac{1}{2},j}\\&-(\rho U)^{n+1}_{i-\frac{1}{2},j}+(\rho V)^{n+1}_{i,j+\frac{1}{2}}-(\rho V)^{n+1}_{i,j-\frac{1}{2}}=0.\end{aligned}\tag{40}$$

Here, $U_{i+\frac{1}{2},j}$ and $V_{i,j+\frac{1}{2}}$ are the volumetric fluxes across the vertical and horizontal faces of cell Ω_{ij}, respectively, and are given by (see Fig. 2):

$$\begin{aligned}U_{i+\frac{1}{2},j}&=\int\limits_{\xi_{j-\frac{1}{2}}}^{\xi_{j+\frac{1}{2}}}h_{i+\frac{1}{2}}u_{i+\frac{1}{2},j}\,\mathrm{d}\xi,\\V_{i,j+\frac{1}{2}}&=\int\limits_{x_{i-\frac{1}{2}}}^{x_{i+\frac{1}{2}}}\widehat{v}_{i,j+\frac{1}{2}}\,\mathrm{d}x.\end{aligned}\tag{41}$$

Within each finite volume Ω_{ij}, the vertical velocity component u is approximated using a second-order polynomial in ξ:

$$u_{ij}=A_{ij}\xi^2+B_{ij}\xi+C_{ij}.\tag{42}$$

Continuity of velocity and tangential shear stress is enforced at the interface $\xi=\xi_{j+\frac{1}{2}}$ between adjacent cells:

$$u_{ij}\big|_{\xi=\xi_{j+\frac{1}{2}}}=u_{i,j+1}\big|_{\xi=\xi_{j+\frac{1}{2}}},\tag{43}$$

$$\mu_{ij}\frac{\partial u_{ij}}{\partial\xi}\bigg|_{\xi=\xi_{j+\frac{1}{2}}}=\mu_{i,j+1}\frac{\partial u_{i,j+1}}{\partial\xi}\bigg|_{\xi=\xi_{j+\frac{1}{2}}}.\tag{44}$$

Using these conditions and eq. (36) we get

$$A_{ij}=\frac{h_i^2}{\mu_{ij}}\left(\frac{\partial p}{\partial x}+\rho g\right)_{i+\frac{1}{2},j},\tag{45}$$

$$\begin{aligned}&A_{ij}\,\xi^2_{j+\frac{1}{2}}+B_{ij}\,\xi_{j+\frac{1}{2}}+C_{ij}\\&=A_{i,j+1}\xi^2_{j+\frac{1}{2}}+B_{i,j+1}\,\xi_{j+\frac{1}{2}}+C_{i,j+1},\end{aligned}\tag{46}$$

$$\begin{aligned}&\mu_{ij}\left(2A_{ij}\,\xi_{j+\frac{1}{2}}+B_{ij}\right)\\&=\mu_{i,j+1}\left(2A_{i,j+1}\,\xi_{j+\frac{1}{2}}+B_{i,j+1}\right).\end{aligned}\tag{47}$$

We assume that the combined pressure gradient and gravitational force term $\left(\frac{\partial p}{\partial x}+\rho g\right)$ is approximately constant within each cell in the ξ direction:

$$\left(\frac{\partial p}{\partial x}+\rho g\right)_{i+\frac{1}{2},j}\approx\left(\frac{\partial p}{\partial x}+\overline{\rho}g\right)_{i+\frac{1}{2}}.\tag{48}$$

Following this condition and eq. (47) we have $B_{ij}=0$. Denoting $A_{ij}=a_{ij}h^2\left(\frac{\partial p}{\partial x}+\overline{\rho}g\right)_{i+\frac{1}{2}}$ and $C_{ij}=c_{ij}h^2\left(\frac{\partial p}{\partial x}+\overline{\rho}g\right)_{i+\frac{1}{2}}$ we get

$$\begin{aligned}ca_{ij}&=\frac{1}{2\mu_{ij}},\\c_j&=(a_{j+1}-a_j)\xi^2_{j+\frac{1}{2}}+c_{j+1}.\end{aligned}\tag{49}$$

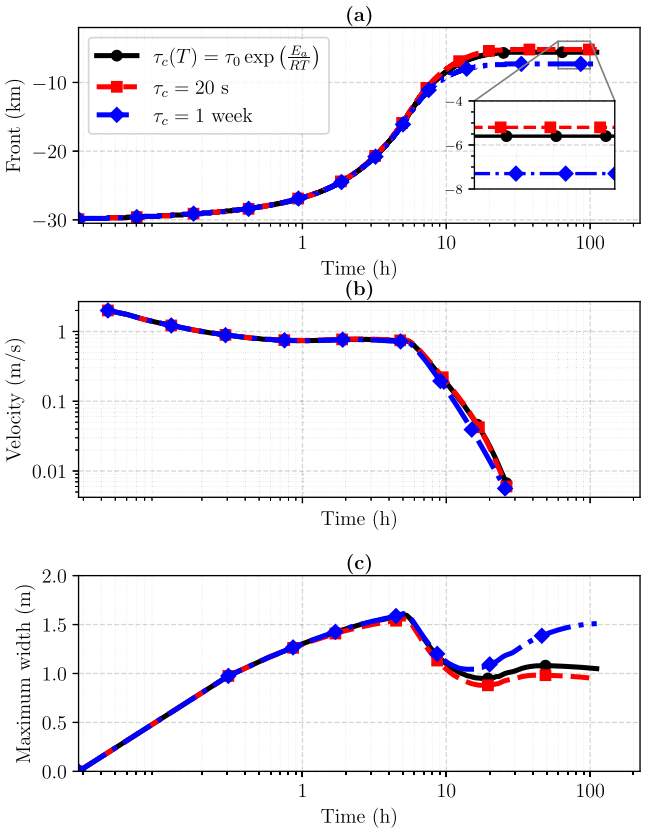

Figure 7. Evolution of dike front (a), ascent velocity (b) and maximum dike width (c) for different crystallization kinetics: temperature-dependent relaxation time given by (26), and constant relaxation times of $\tau_c = 20$s and $\tau_c = 1$week(= 168 hr).

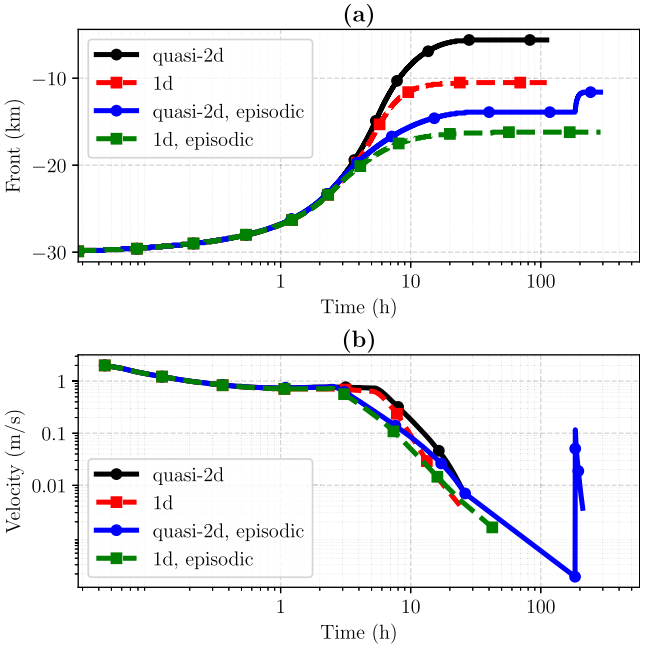

Figure 8. Dike front evolution (a) and ascent velocity (b) for the quasi-2-D model and the 1-D approximation. For all magma injected steadily in first 15000 s (4 hr), the quasi-2-D model (black) predicts a faster ascent and shallower final arrest depth due to transverse gradients in temperature and viscosity, which are absent in the 1-D model (red). Results for the episodic injection case with the same total magma volume injected are shown by the blue (quasi-2-D) and green (1-D) lines. For these, half the volume was injected over the first 2 hr, followed by a 1 week (168 hr) pause before the rest was injected over 2 hr.

Using no-slip condition (9) we have $c_{N_y} = a_{N_y}$. Together, these conditions uniquely determine the polynomial coefficients a_j and c_j in each cell. Finally, we get

$$U_{i+\frac{1}{2},j} = \lambda_{i+\frac{1}{2},j} h^3_{i+\frac{1}{2}} \left(\frac{\partial p}{\partial x} + \overline{\rho} g\right)_{i+\frac{1}{2}}, \tag{50}$$

where

$$\lambda_{i+\frac{1}{2},j} = \int_{\xi_{j-\frac{1}{2}}}^{\xi_{j+\frac{1}{2}}} \left(a_j \xi^2 + c_j\right) \mathrm{d}\xi. \tag{51}$$

The discrete form of the integrated mass balance eq. (39) is obtained by summing eq. (40) across all cells in the ξ direction:

$$\frac{(\overline{\rho}_i h_i)^{n+1} - (\overline{\rho}_i h_i)^n}{\Delta t} \Delta x + M_{i+\frac{1}{2}} - M_{i-\frac{1}{2}} = 0. \tag{52}$$

Here, $M_{i+\frac{1}{2}}$ is a total mass rate between adjacent control volumes along the vertical (x) direction

$$\begin{aligned} cM_{i+\frac{1}{2}} &= \sum_{j=1}^{N_y} \rho_{ij} U_{i+\frac{1}{2},j} \\ &= \left(\sum_{j=1}^{N_y} \rho_{ij} \lambda_{i+\frac{1}{2},j}\right) h^3_{i+\frac{1}{2}} \left(\frac{\partial p}{\partial x} + \overline{\rho} g\right)_{i+\frac{1}{2}}. \end{aligned} \tag{53}$$

The pressure gradient term $\frac{\partial p}{\partial x}$ is approximated using a central difference scheme as $\left(\frac{\partial p}{\partial x}\right)_{i+\frac{1}{2}} \approx \frac{p_{i+1} - p_i}{\Delta x}$.

After each time step, magma properties at t^{n+1}—including density, viscosity and equilibrium crystallinity—are updated using state variables from the previous time level t^n:

$$f^{n+1} = f(p^n, T^n, \alpha^n). \tag{54}$$

Then, these updated parameters are used to evaluate the velocity coefficients in eq. (50).

The elasticity eq. (1) is discretized using the Displacement Discontinuity Method. For this, we assume that the pressure and the half-width are represented as piecewise constant functions, so that the integral can be evaluated analytically and written in closed form

$$p_i = \sigma_{\mathrm{lith},i} + \sigma_{\mathrm{coh}}(w_i) + \sum_j E_{ij} h_j, \tag{55}$$

where E_{ij} is the elastic contribution of segment with centre x_j on segment with centre x_i

$$E_{ij} = \frac{E'}{2\pi} \left(\frac{1}{x_i - x_{j+\frac{1}{2}}} - \frac{1}{x_i - x_{j-\frac{1}{2}}}\right). \tag{56}$$

Let $\boldsymbol{p}$ be the magma pressure vector, $\boldsymbol{h}$ the of half-width vector and $\mathbb{E}$ the elasticity matrix computed via eq. (56). The matrix $\mathbb{A} = A(\boldsymbol{p}^{k+1}, \boldsymbol{h}^k)$ arises from eq. (52) and is defined componentwise as

$$[A\boldsymbol{p}]_i = M_{i+\frac{1}{2}}(\boldsymbol{p}^{k+1}, \boldsymbol{h}^k) - M_{i-\frac{1}{2}}(\boldsymbol{p}^{k+1}, \boldsymbol{h}^k). \tag{57}$$

After discretization, we arrive at the following coupled linear system, solved via fixed-point iteration with respect to index k, to compute the updated pressure $\boldsymbol{p}^{n+1}$ and half-width $\boldsymbol{h}^{n+1}$:

$$\begin{pmatrix} \mathbb{I} & -\left[\mathbb{E} + \boldsymbol{\sigma}'_{\mathrm{coh}}(2\boldsymbol{h}^k)\right] \\ \mathbb{A} & \frac{\overline{\rho}^{n+1}\Delta x}{\Delta t}\mathbb{I} \end{pmatrix} \begin{pmatrix} \boldsymbol{p}^{k+1} \\ \boldsymbol{h}^{k+1} \end{pmatrix} = \begin{pmatrix} \boldsymbol{\sigma}_0 + \boldsymbol{\sigma}_{\mathrm{coh}}(2\boldsymbol{h}^k) \\ \frac{\overline{\rho}^n \Delta x}{\Delta t}\boldsymbol{h}^n + \frac{Q_m}{2}\delta(x_{\mathrm{ch}}) \end{pmatrix}. \tag{58}$$

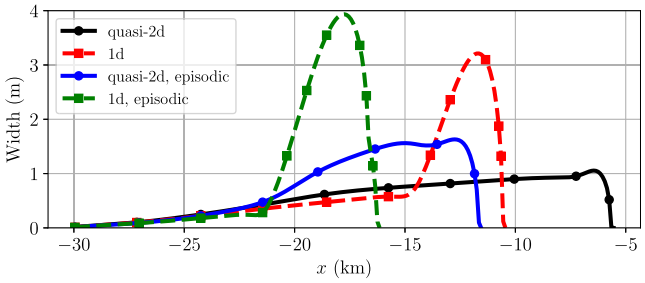

Figure 9. Dike width profiles for the quasi-2-D model (black) and the 1-D approximation (red) at approximately 100 hr after injection initiation, and for the episodic injection case at 288 hr (blue and green). This corresponds to the arrested state shown in Fig. 8(a).

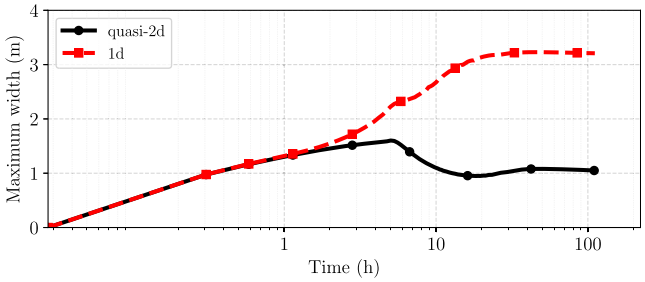

Figure 10. Evolution of maximum dike width for the quasi-2-D model (black) and the 1-D approximation (red).

The term $\frac{Q_m}{2}\delta(x_{\rm ch})$ originates from the inlet boundary condition at the magma chamber (10). Since the elasticity matrix $\mathbb{E}$ is dense, directly solving the coupled system (58) is computationally expensive. To reduce cost, $\mathbb{E}\boldsymbol{h}^{k+1}$ is approximated by a decomposition:

$$\mathbb{E}\boldsymbol{h}^{k+1} \approx \mathbb{E}_1\boldsymbol{h}^{k+1} + \mathbb{E}_2\boldsymbol{h}^{k}, \tag{59}$$

where $\mathbb{E}_1$ is a tridiagonal matrix and $\mathbb{E}_2 = \mathbb{E} - \mathbb{E}_1$. This approximation yields a sparse system matrix.

After computing the updated pressure $\boldsymbol{p}^{n+1}$ and half-width $\boldsymbol{h}^{n+1}$, the horizontal fluxes U are evaluated using eq. (50). These fluxes are used in the discrete mass eq. (40) to compute the transverse fluxes V via an upwind scheme.

The evolution of crystal content is described by the mass conservation equation for the crystal phase (3). Its discretization over the control volume Ω_{ij} yields:

$$\begin{aligned}&\tfrac{(\alpha_c\rho_c h)^{n+1}_{ij}-(\alpha_c\rho_c h)^{n}_{ij}}{\Delta t}\Delta x\Delta\xi + (\alpha_c\rho_c U)^{n+1}_{i+\frac12,j}\\ &-(\alpha_c\rho_c U)^{n+1}_{i-\frac12,j} + (\alpha_c\rho_c V)^{n+1}_{i,j+\frac12} - (\alpha_c\rho_c V)^{n+1}_{i,j-\frac12}\\ &\quad = -(1-\alpha)\rho_c\tfrac{\beta-\beta_{\rm eq}}{\tau_c}h_i\Delta x\Delta\xi,\end{aligned} \tag{60}$$

where $\alpha_c = (1-\alpha)\beta$ from (21).

The energy balance eq. (37) is discretized in a manner analogous to the mass balance equation. Integrating over the control volume Ω_{ij} gives the following discrete form:

$$\begin{aligned}&\tfrac{(\rho C h T)^{n+1}_{ij}-(\rho C h T)^{n}_{ij}}{\Delta t}\Delta x\Delta\xi + (\rho C T U)^{n+1}_{i+\frac12,j}\\ &-(\rho C T U)^{n+1}_{i-\frac12,j} + (\rho C T V)^{n+1}_{i,j+\frac12} - (\rho C T V)^{n+1}_{i,j-\frac12}\\ &= \tfrac{\Delta x}{h_i}\left[\left(k\frac{\partial T}{\partial\xi}\right)_{i,j+\frac12} - \left(k\frac{\partial T}{\partial\xi}\right)_{i,j-\frac12}\right] +\\ &+\tfrac{\mu_{ij}}{h_i}\left(\frac{\partial u}{\partial\xi}\right)^2_{ij}\Delta x\Delta\xi + h_i(\Phi_c)_{ij}\Delta x\Delta\xi.\end{aligned} \tag{61}$$

The conduction heat flux is approximated using a central difference scheme, $\left(k\frac{\partial T}{\partial\xi}\right)_{i,j+\frac12} \approx k\frac{T_{i,j+1}-T_{i,j}}{\xi_{j+1}-\xi_j}$. The heat conduction equation in the surrounding rock (19) is discretized similarly:

$$\begin{aligned}&\tfrac{(\rho_r C_r T_r)^{n+1}_j-(\rho_r C_r T_r)^{n}_j}{\Delta t}\Delta x\Delta y_r\\ &= \left(k_r\frac{\partial T_r}{\partial y}\right)_{j+\frac12}\Delta x - \left(k_r\frac{\partial T_r}{\partial y}\right)_{j-\frac12}\Delta x.\end{aligned} \tag{62}$$

The linear systems (61) and (62) are solved efficiently by decomposition into tridiagonal systems along the transverse directions ξ and y_r, significantly reducing computational cost.

The discretized equations are assembled into a semi-implicit algorithm that updates all variables in a consistent sequence. Fig. 3 presents the overall structure of the method, outlining the update sequence for pressure, fracture width, velocity field and thermodynamic variables.

4 SIMULATION RESULTS

4.1 Verification

We verified our numerical method by comparing simulation results to the classical Roper–Lister solution (Roper & Lister 2007), which describes buoyancy-driven propagation of a viscous, isothermal fluid in an elastic half-space. Mesh sensitivity studies confirmed numerical convergence, and further details of these tests are provided in the Section S2 of the Supplementary Material.

4.2 Crystal kinetics

The simulation results for the basic set of parameters listed in Table 1 are shown in Fig.4 The first, second and third panels illustrate the temperature, crystal content and viscosity of magma in the dike after arrest. At the margin of the dike the magma cools rapidly and crystallization is suppressed, leading to formation of a glassy chilled margin because the rate of crystal growth decreases exponentially with decreasing temperature (see eq. 26). Further inside the dike a localized area of crystal-rich magma develops. In contrast, the dike core remains hotter and less crystalline during the whole period of magma propagation. As the arrested magma cools, the interior of the dike also progressively crystallizes. The lateral variations in magma rheology during ascent due to variations in crystallinity and temperature across the dike, significantly modifies the flow structure: the vertical velocity profiles (Fig. 4 right panel) reveal a marked reduction in velocity near the walls, deviating from the classical parabolic (Poiseuille) profile.

The presence of a chilled (glassy) margin only occurs when the relaxation time in eq. (25) depends on the temperature. This effect is absent in models that assume a constant crystallization relaxation time, τ_c. Fig. 5 demonstrates a simulation employing a small constant $\tau_c = 20$ s, which makes crystallization sufficiently quick to serve as an approximation for the equilibrium condition where $\beta = \beta_{\rm eq}$. In this case, no distinct chilled margin is formed, and crystal concentration and viscosity change more gradually. Additionally, Fig. 6 presents a simulation with a much larger constant relaxation time, $\tau_c = 1$ week, showing a further reduction in gradients and an even more uniform distribution of crystals and viscosity across the dike. Notably, for larger crystal growth times, the dike front arrests at a greater depth (see Fig. 7a), even though the total crystal content is reduced. This occurs because crystallization releases latent heat, increasing the magma temperature within the dike, as demonstrated

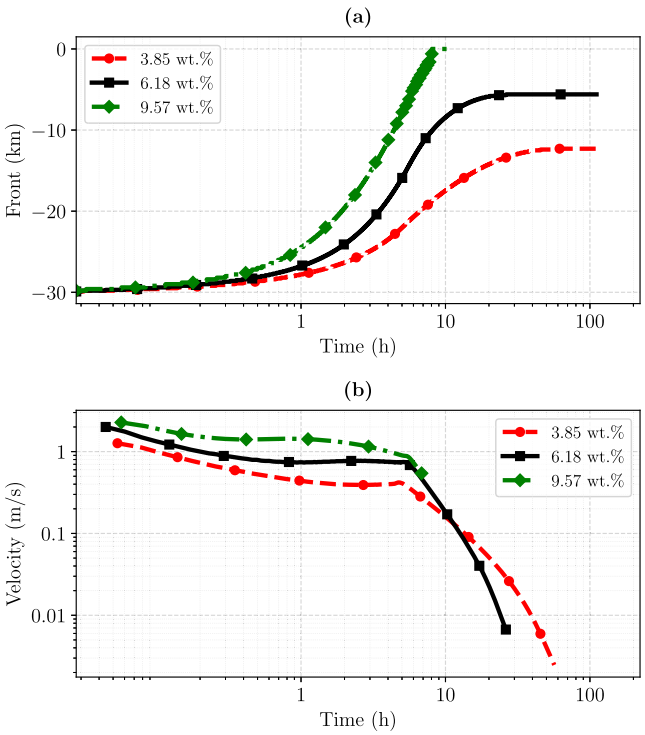

Figure 11. Dike front evolution (a) and ascent velocity (b) for different initial water contents (3.85 wt. per cent, 6.18 wt. per cent and 9.57 wt. per cent). Increased water content leads to faster propagation due to significantly lower melt viscosity, as predicted by the Giordano viscosity model (Giordano *et al.* 2008).

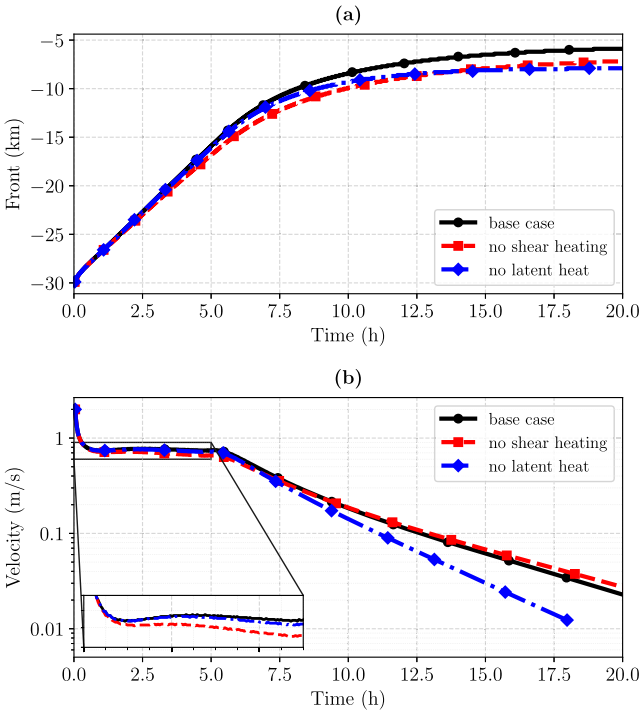

Figure 12. Dike front evolution (a) and ascent velocity (b) for the base case (see Fig. 4 in the main text), and two modified scenarios: without shear heating and without latent heat. Shear heating has the strongest effect at early times, when the ascent velocity is high. Later, the influence of latent heat becomes more significant. In both modified cases, the final propagation depth is lower than in the base case.

by the hotter dike core for simulations with shorter τ_c that have more crystallization on the dike margins (Figs 5 and 6). Thus, despite the lower total crystal content, the dike core is cooler and more viscous for the larger crystal growth time. The magma of the dike tail, which is hotter than the magma in the head, remains more mobile, allowing continued flow towards the tip. As a result, the dike head width continues to increase despite front stagnation (see Fig. 7c). This is preceded by an initial increase in width caused by magma injection from the chamber, and a subsequent decrease due to the increasing length of the dike.

4.3 Comparison of quasi-2-D and 1-D models

In this section we compared the quasi-2-D model with a simplified 1-D approximation to demonstrate the effect of the non-Poiseuille velocity profile on dike propagation. In the 1-D model, the magma temperature is artificially maintained uniform across the dike cross-section by imposing a high thermal conductivity ($k = 2000$ W (m·K)$^{-1}$). This eliminates lateral temperature gradients, which are essential for generating non-Poiseuille velocity profiles and capturing 2-D-flow behaviour. Fig. 8(a) shows the evolution of the dike tip (front) over time for the quasi-2-D model (black line) and the 1-D approximation (red line). The 1-D model exhibits higher average viscosity, lower ascent velocity and earlier arrest compared to the quasi-2-D simulation. In contrast, the quasi-2-D model resolves the development of a hot, low-viscosity core that sustains vertical transport even as the dike margins cool and crystallize. Additionally, the dike width profiles after dike arrest in Fig. 9 highlight structural differences between the two models. The 1-D model shows a sharp increase in width near the front that formed following rapid dike arrest by the continued addition of magma from below, inflating the head of the dike (Fig. 10). The quasi-2-D model produces a smoother and narrower shape.

The difference between the quasi-2-D and 1-D approaches becomes more evident in the case of episodic magma injection from the chamber into the dike. We performed simulations for both quasi-2-D and 1-D models with the same total magma mass, but supplied in two equal pulses separated by a one-week interval. During the time between the two pulses, magma in the dike cools and the dike arrests (see Fig. 8). After the second pulse, when magma reaches the tip, the quasi-2-D model predicts that the dike front continues to move forward (see the blue line in Fig. 8a). In the 1-D case (green line), the front remains stationary and only the width increases near the tip.

4.4 Parametric analysis

Fig. 11 illustrates the effect of initial water content on dike propagation. We assume that in all simulations, magmas are generated at the same depth, thus, have the same saturation pressure. According to the solubility diagram, magmas with higher water content has lower CO_2 content (see degassing paths in Section S1 of the Supplementary Material). Higher water content reduces melt viscosity and increases buoyancy of the magma at shallow depth due to volatile exsolution, thereby enhancing magma mobility and promoting faster ascent. This behaviour is evident in both the dike front position and ascent velocity: simulations with greater water content exhibit more rapid propagation. However, the velocity in

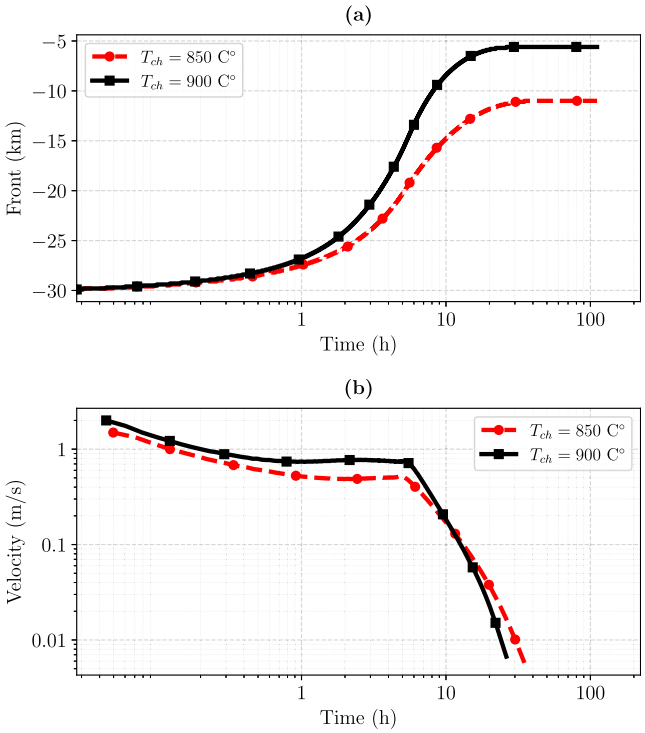

Figure 13. Dike front evolution (a) and ascent velocity (b) for two initial magma temperatures: $T_{\mathrm{ch}} = 850°\mathrm{C}$ and $T_{\mathrm{ch}} = 900°\mathrm{C}$.

wetter systems also declines more steeply at later times, due to accelerated degassing-induced crystallization and more shallow arrest depth corresponding to cooler host rocks.

To illustrate the influence of shear heating and latent heat of crystallization, we performed two additional simulations: one without shear heating and another without latent heat release. The results (Fig. 12) show that shear heating significantly affects the early stage of dike propagation, when the ascent velocity is high. At later times, the latent heat of crystallization has a greater impact, slowing down cooling and prolonging propagation. In both cases, the final ascent depth is lower than in the base scenario, where both effects are included.

Fig. 13 illustrates the effect of initial magma temperature on dike propagation. Simulations with higher T_{ch} show faster ascent and shallower arrest, which reflects the strong temperature dependence of magma viscosity. Hotter magma retains its fluidity over longer distances, delaying crystallization and maintaining lower resistance to flow.

Additional sensitivity tests on Young's modulus and fracture toughness are provided in Section S3 of the Supplementary Material, showing that dike propagation is weakly affected by mechanical parameters within the tested range. Abdullin *et al.* (2024) showed that the arrest depth and the dike propagation dynamics are also strongly affected by the total mass of the injected magma, which has not been varied in this study.

5 DISCUSSION AND CONCLUSION

In this study, we developed a quasi-2-D model of dike propagation that resolves transverse variations in magma properties across the dike width. Capturing these gradients is critical: for typical dike widths ($\sim$ 1 m), temperature differences of up to 100 °C can arise between the centre and the walls. Such thermal gradients drive spatially heterogeneous crystallization, which modifies magma viscosity. Our simulations demonstrate that viscosity near the dike walls increases due to localized cooling and crystal growth, while the core remains hotter and less crystalline. This contrast leads to significant deviations from classical Poiseuille flow, with velocity profiles becoming increasingly plug-like in the presence of crystal-rich wall zones.

We show that 1-D models, which average parameters across the cross-section, underestimate magma mobility and predict earlier arrest due to overestimated effective viscosity. By contrast, the quasi-2-D approach allows hotter, low-viscosity magma to continue feeding the flow, bypassing crystallized wall zones via dynamic velocity redistribution.

To capture time-dependent crystallization, we incorporated a non-equilibrium kinetic model with a temperature-dependent relaxation timescale. This enables more physically realistic of latent heat release and rheological feedbacks during crystallization, particularly near the dike front.

Future research should address the coupled kinetics of crystal nucleation and growth under non-equilibrium thermal conditions. Crystal content and texture may be far from equilibrium during rapid ascent; resolving these effects is crucial for predicting the development of phenocrysts, microlites and the resulting mechanical properties of the chilled margin (Melnik *et al.* 2011).

A significant limitation of the present model is its simplified treatment of gas phase transport. While vertical escape of exsolved gas becomes important mainly near the arrest depth, simulating post-arrest gas migration and possible interactions with wall rocks could clarify the links between dike intrusion, late-stage degassing and secondary hydrothermal features.

Another limitation concerns the treatment of heat transfer (see eq. 11). Assuming conduction as the dominant process is reasonable for deeper crustal levels, but as the dike approaches the surface it may intersect hydrothermal systems, where advective heat transfer could become important and significantly influence the thermal evolution. Capturing such effects would require inclusion of a fluid filtration equation for the host rock, greatly increasing the computational complexity of the model, and is therefore left for future research.

A more realistic account of magma supply requires dynamic coupling between the magma chamber and the propagating dike. Time-dependent chamber pressure, depletion effects and feedbacks from dike propagation are not included in our approach, but can strongly influence the mass and timing of eruptive events (Melnik & Sparks 2002; Rivalta 2010).

Our model does not account for heterogeneous or anisotropic tectonic stresses. While uniform far-field stresses can be included by adjusting rock density, more complex stress fields and elastic variations require approaches that allow non-vertical dike trajectories. Additionally, the level of neutral buoyancy can influence dike propagation. Near this level, dikes may stall, propagate laterally or transition into sills, especially when combined with rigidity contrasts or external stress fields (Maccaferri *et al.* 2011, 2019). Because the 2-D model assumes a constant dike breadth, it cannot resolve variations that arise in real systems. 3-D simulations show that dike breadth can vary significantly depending on governing parameters (Möri & Lecampion 2022).

Finally, experimental and modelling studies highlight that both viscoelastic relaxation of thermally weakened host rocks and shear-induced dilation of partially crystalline mush zones play critical roles in controlling magma migration and reservoir deformation.

Time-dependent viscoelastic and dilatant responses can sustain deformation even after magma injection ceases, affect dike propagation pathways and facilitate melt transport through dense crystal mush. Incorporating these rheological complexities is essential for accurately predicting fracture evolution and heat transfer in deep or high-temperature magmatic systems (Alshembari *et al.* 2023; Ryan *et al.* 2025).

ACKNOWLEDGMENTS

This work builds on the 1-D code and results presented in Abdullin *et al.* (2024) which resulted from research funded by BHP.

SUPPORTING INFORMATION

Supplementary data are available at *GJIRAS* online.

suppl_data
Please note: Oxford University Press is not responsible for the content or functionality of any supporting materials supplied by the authors. Any queries (other than missing material) should be directed to the corresponding author for the paper.

DATA AVAILABILITY

The simulation code are available at https://github.com/rustamNSU/magma-dikes-2d-flow

REFERENCES

Abdullin, R., Melnik, O., Rust, A., Blundy, J., Lgotina, E. & Golovin, S., 2024. Ascent of volatile-rich felsic magma in dykes: a numerical model applied to deep-sourced porphyry intrusions, *Geophys. J. Int.,* **236**(3), 1863–1876.

Acocella, V., Ripepe, M., Rivalta, E., Peltier, A., Galetto, F. & Joseph, E., 2024. Towards scientific forecasting of magmatic eruptions, *Nat. Rev. Earth Environ.,* **5**(1), 5–22.

Alshembari, R., Hickey, J., Williamson, B.J. & Cashman, K., 2023. Unveiling the rheological control of magmatic systems on volcano deformation: The interplay of poroviscoelastic magma-mush and thermo-viscoelastic crust, *J. geophys. Res.: Solid Earth,* **128**(7), e2023JB026625.

Baykin, A., Abdullin, R., Dontsov, E. & Golovin, S., 2023. Two-dimensional models for waterflooding induced hydraulic fracture accounting for the poroelastic effects on a reservoir scale, *Geoenergy Sci. Eng.,* **224,** 211600.

Carter, L.C., Williamson, B.J., Tapster, S.R., Costa, C., Grime, G.W. & Rollinson, G.K., 2021. Crystal mush dykes as conduits for mineralising fluids in the Yerington Porphyry Copper District, Nevada, *Commun. Earth Environ.,* **2**(1), 59.

Costa, A., Caricchi, L. & Bagdassarov, N., 2009. A model for the rheology of particle-bearing suspensions and partially molten rocks, *Geochem. Geophys. Geosyst.,* **10**(3).

Crouch, S.L., Starfield, A.M. & Rizzo, F., 1983. Boundary element methods in solid mechanics, *J. Appl. Mech.,* **50,** 704.

Davis, T., Rivalta, E., Smittarello, D. & Katz, R.F., 2023. Ascent rates of 3-D fractures driven by a finite batch of buoyant fluid, *J. Fluid Mech.,* **954,** A12.

Dirksen, O., Humphreys, M.C.S., Pletchov, P., Melnik, O., Demyanchuk, Y., Sparks, R.S.J. & Mahony, S., 2006. The 2001–2004 dome-forming eruption of Shiveluch Volcano, Kamchatka: Observation, petrological investigation and numerical modelling, *J. Volc. Geotherm. Res.,* **155**(3–4), 201–226.

Dontsov, E.V., 2016. Propagation regimes of buoyancy-driven hydraulic fractures with solidification, *J. Fluid Mech.,* **797,** 1–28.

Garagash, D.I., 2019. Cohesive-zone effects in hydraulic fracture propagation, *J. Mech. Phys. Solids,* **133,** 103727.

Ghiorso, M.S. & Gualda, G.A., 2015. An H_2O–CO_2 mixed fluid saturation model compatible with rhyolite-MELTS, *Contrib. Mineral. Petrol.,* **169,** 1–30.

Giordano, D., Russell, J.K. & Dingwell, D.B., 2008. Viscosity of magmatic liquids: a model, *Earth planet. Sci. Lett.,* **271**(1–4), 123–134.

Golovin, S.V. & Baykin, A.N., 2018. Influence of pore pressure on the development of a hydraulic fracture in poroelastic medium, *Int. J. Rock Mech. Mining Sci.,* **108,** 198–208.

Griffith, A.A., 1921. VI. the phenomena of rupture and flow in solids, *Phil. Trans. R. Soc. Lond.,* **221**(582-593), 163–198.

Gudmundsson, A., 2006. How local stresses control magma-chamber ruptures, dyke injections, and eruptions in composite volcanoes, *Earth-Sci. Rev.,* **79**(1–2), 1–31.

Hammer, J.E. & Rutherford, M.J., 2002. An experimental study of the kinetics of decompression-induced crystallization in silicic melt, *J. geophys. Res.: Solid Earth,* **107**(B1), ECV 8–1-ECV 8-24.

Iacovino, K., Matthews, S., Wieser, P.E., Moore, G. & Bégué, F., 2021. Vesical part I: an open-source thermodynamic model engine for mixed volatile (H_2O-CO_2) solubility in silicate melts, *Earth Space Sci.,* **8**(11), e2020EA001584.

Irwin, G.R., 1957. Analysis of stresses and strains near the end of a crack traversing a plate, *J. Appl. Mech.,* **24**(3), 361–364.

La Spina, G., Burton, M. & de' Michieli Vitturi, M., 2015. Temperature evolution during magma ascent in basaltic effusive eruptions: A numerical application to Stromboli volcano, *Earth planet. Sci. Lett.,* **426,** 89–100.

Lister, J.R. & Kerr, R.C., 1991. Fluid-mechanical models of crack propagation and their application to magma transport in dykes, *J. geophys. Res.: Solid Earth,* **96**(B6), 10 049–10 077.

Maccaferri, F., Bonafede, M. & Rivalta, E., 2011. A quantitative study of the mechanisms governing dike propagation, dike arrest and sill formation, *J. Volc. Geotherm. Res.,* **208**(1–2), 39–50.

Maccaferri, F., Smittarello, D., Pinel, V. & Cayol, V., 2019. On the propagation path of magma-filled dikes and hydrofractures: the competition between external stress, internal pressure, and crack length, *Geochem. Geophys. Geosyst.,* **20**(4), 2064–2081.

Melnik, O. & Sparks, R.S., 1999. Nonlinear dynamics of lava dome extrusion, *Nature,* **402**(6757), 37–41.

Melnik, O. & Sparks, R.S.J., 2002. *Dynamics of Magma Ascent and Lava Extrusion at Soufrière Hills Volcano, Montserrat,* vol. 21, Geological Society of London. doi:10.1144/GSL.MEM.2002.021.

Melnik, O.E., Blundy, J.D., Rust, A.C. & Muir, D.D., 2011. Subvolcanic plumbing systems imaged through crystal size distributions, *Geology,* **39**(4), 403–406.

Möri, A. & Lecampion, B., 2022. Three-dimensional buoyant hydraulic fractures: constant release from a point source, *J. Fluid Mech.,* **950,** A12.

Rivalta, E., 2010. Evidence that coupling to magma chambers controls the volume history and velocity of laterally propagating intrusions, *J. geophys. Res.: Solid Earth,* **115**(B7). doi:10.1029/2009JB006922.

Rivalta, E. & Chamberlain, K., 2025. The influence of crustal stress on the pathways and evolution of magmas ascending by dyking, *ESS Open Archive*.

Rivalta, E., Taisne, B., Bunger, A.P. & Katz, R.F., 2015. A review of mechanical models of dike propagation: Schools of thought, results and future directions, *Tectonophysics,* **638,** 1–42.

Roper, S. & Lister, J., 2007. Buoyancy-driven crack propagation: the limit of large fracture toughness, *J. Fluid Mech.,* **580,** 359–380.

Roper, S.M. & Lister, J.R., 2005. Buoyancy-driven crack propagation from an over-pressured source, *J. Fluid Mech.,* **536,** 79–98.

Rubin, A.M., 1995. Propagation of magma-filled cracks, *Annu. Rev. Earth Planet. Sci.,* **23**(1), 287–336.

Ryan, A.G., Hansen, L.N., Dillman, A., Pistone, M., Zimmerman, M.E. & Williams, S.A., 2025. Shear-induced dilation and dike formation during mush deformation, *Earth planet. Sci. Lett.,* **651,** 119164.

Tsepelev, I., Ismail-Zadeh, A. & Melnik, O., 2020. Lava dome morphology inferred from numerical modelling, *Geophys. J. Int.,* **223**(3), 1597–1609.

Zhang, Y., Ni, H. & Chen, Y., 2010. Diffusion data in silicate melts, *Rev. Mineral. Geochem.,* **72,** 311–408.

APPENDIX A: REDUCTION OF NAVIER–STOKES EQUATIONS

To illustrate reduction of Navier–Stokes eqs (4)–(6) to system of eqs (16)–(18), consider the following dimensionless parameters

$$\begin{aligned} u &= U\tilde{u}, \quad v = V\tilde{v}, \quad x = L\tilde{x}, \quad y = H\tilde{y}, \\ t &= T\tilde{t}, \quad \rho = R\tilde{\rho}, \quad p = P\tilde{p}, \quad \mu = M\tilde{\mu}, \end{aligned} \tag{A1}$$

and

$$U = \frac{L}{T}, \quad V = \frac{H}{T}, \quad \varepsilon = \frac{H}{L}, \tag{A2}$$

where $\varepsilon \ll 1$.

$$\frac{R}{T}\left(\frac{\partial\tilde{\rho}}{\partial\tilde{t}} + \frac{\partial(\tilde{\rho}\tilde{u})}{\partial\tilde{x}} + \frac{\partial(\tilde{\rho}\tilde{v})}{\partial\tilde{y}}\right) = 0, \tag{A3}$$

$$\begin{aligned} &\frac{RL}{T^2}\left(\frac{\partial(\tilde{\rho}\tilde{u})}{\partial\tilde{t}} + \frac{\partial(\tilde{\rho}\tilde{u}\tilde{u})}{\partial\tilde{x}} + \frac{\partial(\tilde{\rho}\tilde{v}\tilde{u})}{\partial\tilde{y}}\right) = -\frac{P}{L}\frac{\partial\tilde{p}}{\partial\tilde{x}} \\ &-R\tilde{\rho}g + \frac{M}{LT}\left[\frac{\partial}{\partial\tilde{x}}\left(2\tilde{\mu}\frac{\partial\tilde{u}}{\partial\tilde{x}}\right) + \frac{\partial}{\partial\tilde{y}}\left(\tilde{\mu}\frac{\partial\tilde{v}}{\partial\tilde{x}}\right)\right] \\ &+\frac{ML}{H^2T}\frac{\partial}{\partial\tilde{y}}\left(\tilde{\mu}\frac{\partial\tilde{u}}{\partial\tilde{y}}\right), \end{aligned} \tag{A4}$$

$$\begin{aligned} &\frac{RH}{T^2}\left(\frac{\partial(\tilde{\rho}\tilde{v})}{\partial\tilde{t}} + \frac{\partial(\tilde{\rho}\tilde{u}\tilde{v})}{\partial\tilde{x}} + \frac{\partial(\tilde{\rho}\tilde{v}\tilde{v})}{\partial\tilde{y}}\right) = -\frac{P}{H}\frac{\partial\tilde{p}}{\partial\tilde{y}} \\ &+\frac{M}{HT}\left[\frac{\partial}{\partial\tilde{x}}\left(\tilde{\mu}\frac{\partial\tilde{u}}{\partial\tilde{y}}\right) + \frac{\partial}{\partial\tilde{y}}\left(2\tilde{\mu}\frac{\partial\tilde{v}}{\partial\tilde{y}}\right)\right] \\ &+\frac{MH}{L^2T}\frac{\partial}{\partial\tilde{x}}\left(\tilde{\mu}\frac{\partial\tilde{v}}{\partial\tilde{x}}\right). \end{aligned} \tag{A5}$$

Following the elasticity eq. (1)

$$P\tilde{p} = RLg\tilde{\sigma}_{\text{lith}} + \frac{EH}{L}\tilde{p}_e, \tag{A6}$$

which gives

$$P = RLg. \tag{A7}$$

Using definitions for Reynolds and Froude numbers (see Lister & Kerr 1991)

$$Re = \frac{RHU}{M}, \quad Fr^2 = \frac{L}{gT^2}, \tag{A8}$$

and dividing eq. (A4) by $\frac{ML}{H^2T}$, we get

$$\begin{aligned} &c\varepsilon Re\left(\frac{\partial(\tilde{\rho}\tilde{u})}{\partial\tilde{t}} + \frac{\partial(\tilde{\rho}\tilde{u}\tilde{u})}{\partial\tilde{x}} + \frac{\partial(\tilde{\rho}\tilde{v}\tilde{u})}{\partial\tilde{y}}\right) \\ &= -\varepsilon\frac{Re}{Fr^2}\left(\frac{\partial\tilde{p}}{\partial\tilde{x}} + \tilde{\rho}\right) + \varepsilon^2\left[\frac{\partial}{\partial\tilde{x}}\left(2\tilde{\mu}\frac{\partial\tilde{u}}{\partial\tilde{x}}\right)\right. \\ &\left.+\frac{\partial}{\partial\tilde{y}}\left(\tilde{\mu}\frac{\partial\tilde{v}}{\partial\tilde{x}}\right)\right] + \frac{\partial}{\partial\tilde{y}}\left(\tilde{\mu}\frac{\partial\tilde{u}}{\partial\tilde{y}}\right), \end{aligned} \tag{A9}$$

For the case of small Reynolds number and $Fr \ll 1$, $\varepsilon \ll 1$ we get good agreement with eq. (17). Using the same procedure with eq. (A5) we get

$$\begin{aligned} &\varepsilon^2 Re\left(\frac{\partial(\tilde{\rho}\tilde{v})}{\partial\tilde{t}} + \frac{\partial(\tilde{\rho}\tilde{u}\tilde{v})}{\partial\tilde{x}} + \frac{\partial(\tilde{\rho}\tilde{v}\tilde{v})}{\partial\tilde{y}}\right) = -\frac{Re}{Fr^2}\frac{\partial\tilde{p}}{\partial\tilde{y}} \\ &+\varepsilon\left[\frac{\partial}{\partial\tilde{x}}\left(\tilde{\mu}\frac{\partial\tilde{u}}{\partial\tilde{y}}\right) + \frac{\partial}{\partial\tilde{y}}\left(2\tilde{\mu}\frac{\partial\tilde{v}}{\partial\tilde{y}}\right)\right] + \varepsilon^3\frac{\partial}{\partial\tilde{x}}\left(\tilde{\mu}\frac{\partial\tilde{v}}{\partial\tilde{x}}\right). \end{aligned} \tag{A10}$$

That can be approximated as $\dfrac{\partial\tilde{p}}{\partial\tilde{y}} = 0$. In the same manner, it is easy to get eq. (18) from (6).